



SUBJECT AREAS:

APPLIED PHYSICS

MAGNETIC MATERIALS AND
DEVICES

QUANTUM PHYSICS

MODELLING AND THEORY

Received
15 November 2011Accepted
11 April 2012Published
9 May 2012

Correspondence and
requests for materials
should be addressed to
L.C.L.H. (lloydch@
unimelb.edu.au)

High spatial and temporal resolution wide-field imaging of neuron activity using quantum NV-diamond

L. T. Hall^{1,9}, G. C. G. Beart², E. A. Thomas^{2,8}, D. A. Simpson^{1,9}, L. P. McGuinness¹, J. H. Cole³, J. H. Manton⁴, R. E. Scholten⁵, F. Jelezko⁶, Jörg Wrachtrup⁷, S. Petrou^{9,10,11} & L. C. L. Hollenberg^{1,9}

¹School of Physics, University of Melbourne, Parkville, Victoria 3010, Australia, ²Centre for Neuroscience, University of Melbourne, Parkville, Victoria 3010, Australia, ³Chemical and Quantum Physics, School of Applied Sciences, RMIT University, Melbourne 3001, Australia, ⁴Nonlinear Signal Processing Lab, Melbourne School of Engineering, University of Melbourne, Parkville, Victoria 3010, Australia, ⁵ARC Centre of Excellence in Coherent X-ray Science, School of Physics, University of Melbourne, Victoria 3010, Australia, ⁶Institut für Quantenoptik, Universität Ulm, Ulm D-89073, Germany, ⁷Physikalisches Institut, Universität Stuttgart, 70550 Stuttgart, Germany, ⁸Florey Neuroscience Institutes, Parkville, 3052, Australia, ⁹Centre for Neural Engineering, University of Melbourne, Parkville, Victoria 3010, Australia, ¹⁰Department of Anatomy and Neuroscience, University of Melbourne, Parkville, VIC 3010, Australia, ¹¹Florey Neuroscience Institute, University of Melbourne, Parkville, VIC 3010, Australia.

A quantitative understanding of the dynamics of biological neural networks is fundamental to gaining insight into information processing in the brain. While techniques exist to measure spatial or temporal properties of these networks, it remains a significant challenge to resolve the neural dynamics with subcellular spatial resolution. In this work we consider a fundamentally new form of wide-field imaging for neuronal networks based on the nanoscale magnetic field sensing properties of optically active spins in a diamond substrate. We analyse the sensitivity of the system to the magnetic field generated by an axon transmembrane potential and confirm these predictions experimentally using electronically-generated neuron signals. By numerical simulation of the time dependent transmembrane potential of a morphologically reconstructed hippocampal CA1 pyramidal neuron, we show that the imaging system is capable of imaging planar neuron activity non-invasively at millisecond temporal resolution and micron spatial resolution over wide-fields.

Information processing in the brain is presumed to arise from interactions and correlations across several orders of magnitude of temporal and spatial scales and tens of thousands to billions of computational units. The smallest computational unit is the synapse, with sub-micron structures involved in chemical and electrical signalling. Changes in synaptic dynamics are the basis of learning and memory. While local conditions in the neuron determine signal flow into and out of synapses, complex signal integration and filtering occurs independently in different branches in the dendritic tree (the neuronal input structure). The decision to trigger an output is made in another structure - the axon. Neurons are organized in networks with complex, and largely unknown, connection rules. Networks may contain over a dozen different neuron types, each with their own dynamics and connection rules. Understanding the behaviour of these systems requires understanding the interactions between computational units at different scales in the system^{1,2}.

Current diagnostic techniques are limited in the number of computational units that can be recorded simultaneously at sufficiently high spatial and temporal resolution. New techniques in optogenetics are enabling the manipulation of networks at some of these scales³ however technology to read neuronal networks lags considerably. Voltage sensitive dyes allow readout of the neuron membrane potential, but have poor signal to noise properties and are toxic, making them unsuitable for long term recording^{4,5}. Voltage sensitive fluorescent proteins show promise, but also have poor signal to noise properties and limited temporal and spatial resolution⁶. Direct invasive techniques such as electrophysiological probes are fundamentally limited by the number of electrodes that can be placed in the tissue. Progress in silicon nanowire field-effect transistors have demonstrated sub millisecond temporal resolution, however spatial resolution may ultimately be limited by the distance between adjacent devices^{7–10}.

Our detection method is based on non-invasive magnetic field detection and is therefore fundamentally different to approaches based on detection of electric fields. While the techniques may ultimately complement



each other, our magnetic field based technique will not suffer from some of the drawbacks of electrically-based detection, such as probe positioning with respect to the Debye length and background electrical noise sources at the nanoscale. Furthermore, the detection is inherently non-invasive and issues such as the compatibility of quantum measurements of the NV defect with biological systems are now well established in terms of the low toxicity of diamond and the low photo and microwave powers involved.

The detection set-up we consider consists of a commercial grade single crystal ultra-pure diamond membrane substrate containing a fabricated layer of negatively charged nitrogen-vacancy (NV) defect centres [Fig. 1]. The NV centre is a remarkable optical defect in diamond which allows discrimination of its magnetic sublevels through its fluorescence under illumination. Effectively, each NV is an atomic-sized magnetic field sensor that can be read-out either confocally^{11,12} or via a wide-field CCD¹³, and in a living cellular environment¹⁴. Neurons can be grown directly on the diamond surface¹⁵ whose low toxicity is ideal for biological applications¹⁶. As we show, the ensemble of NV centres provides high sensitivity to the magnetic field fluctuations resulting directly from the transmembrane potentials generated by the neural activity at sub-millisecond time-scales, and the spatial attenuation of the magnetic field at a 100 nm standoff provides micron spatial resolution. This standoff is conservative, as implantation techniques permit the creation of NV centres within a few nm of the diamond surface. Employing a physical model of the hippocampal CA1 pyramidal neuron, developed by Royeck et al¹⁷ and modified by Wimmer et al^{18,19}, we show that the NV detection system is able to non-invasively capture the transmembrane potential activity in a series of near real-time images, with spatial resolution at the level of the individual neural compartments. The data obtained will allow both the planar morphology and function connectivity to be determined. The realisation of this detection system using available technology would represent a significant step forward in measuring and understanding the dynamics of whole-scale neuronal networks.

In what follows, we first outline how transmembrane potentials generate magnetic fields, their typical strength and detection using

the NV centre as a nanoscale magnetometer. We then analyse the detection sensitivity for a single axon case. We experimentally verify this sensitivity by propagating a simulated axon pulse along a micro-wire and detecting the resulting magnetic field signal with a proximate NV centre. Finally, we employ a model of a hippocampal CA1 pyramidal neuron under a typical excitatory regime in which distal dendrites undergo current injections of roughly 2 nA. By direct simulation of the magnetic fields generated at the soma, axon and dendrites in response to this stimulation, we produce the corresponding image output (assuming current CMOS imaging technology²⁰) and determine the effective spatial and temporal resolution of the system.

Results

Sensitivity Analysis. In order to establish our detection regime and required sensitivity we determine theoretically the magnetic fields generated by a transmembrane potential. We model an axon segment as a cylinder of radius a and length L aligned along the z axis [Fig. 2(a)]. These segments form the building blocks of more complicated neuron models to be considered later. Let $\Phi(r, z, t)$ denote the radially-symmetric electric potential at radius r , longitudinal distance z and time t . Approximating the width of the cell membrane to be infinitesimally small, there is a step-change in the potential as it goes from just within the cell, $\Phi(a_-, z, t)$, to just outside the cell, $\Phi(a_+, z, t)$. The transmembrane potential, given by the difference $V_m(z, t) = \Phi(a_-, z, t) - \Phi(a_+, z, t)$, therefore represents the voltage drop across the cell membrane at longitudinal position z and time t . Using data for V_m , one can reconstruct the $\Phi(r, t)$ in the regions inside and outside a given component via the solution of Laplace's equation with boundary conditions set by V_m (see Methods section). By solving for the potentials in both regions, we determine the electric field and hence current densities using Ohm's law, $\mathbf{J}(\mathbf{r}, t) = \sigma(\mathbf{r}, t) \cdot \nabla \Phi(\mathbf{r}, t)$, which is integrated using the Biot-Savart law,

$$\mathbf{B}(\mathbf{r}, t) = \frac{\mu_0}{4\pi} \int \mathbf{J}(\mathbf{r}', t) \times \frac{\mathbf{r} - \mathbf{r}'}{|\mathbf{r} - \mathbf{r}'|^3} d^3 \mathbf{r}' \quad (1)$$

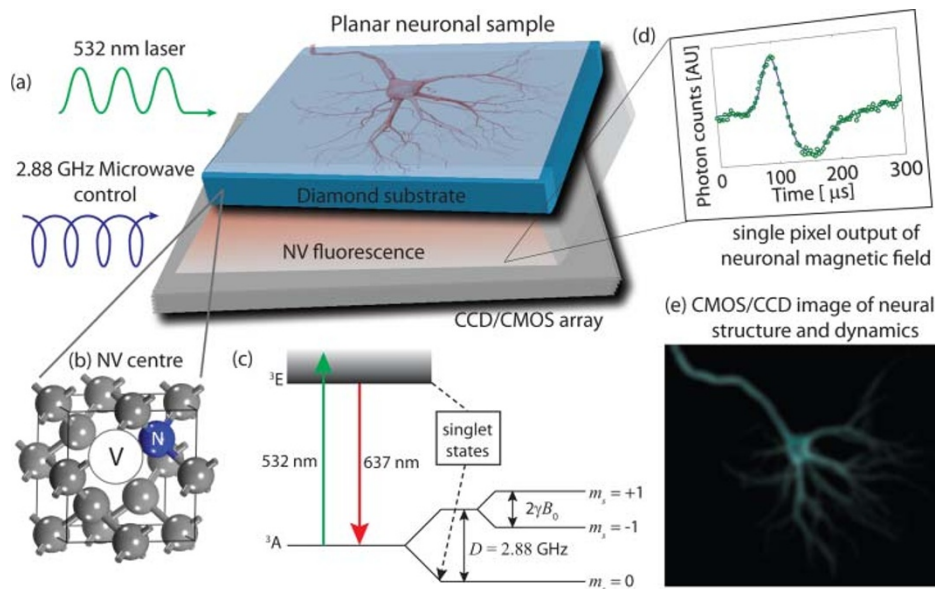


Figure 1 | Schematic of the nitrogen-vacancy (NV) in diamond neuron detection system showing a neural network component (in this case an axon) on a diamond substrate containing fluorescent NV centres. (a) The quantum state may be controlled via application of 2.88 GHz microwave radiation, and is dependent on the strength of the field produced by the axon. (b) Atomic lattice structure of the NV centre. (c). Upon optical excitation at 532 nm, the NV centre spin state may be measured (readout) by monitoring the intensity of the emitted red light using a CCD or CMOS camera. (d) Simulated dynamic output from a single CMOS pixel. (e) By monitoring many pixels, we may obtain a dynamic widefield image of the neural dynamics and network structure.

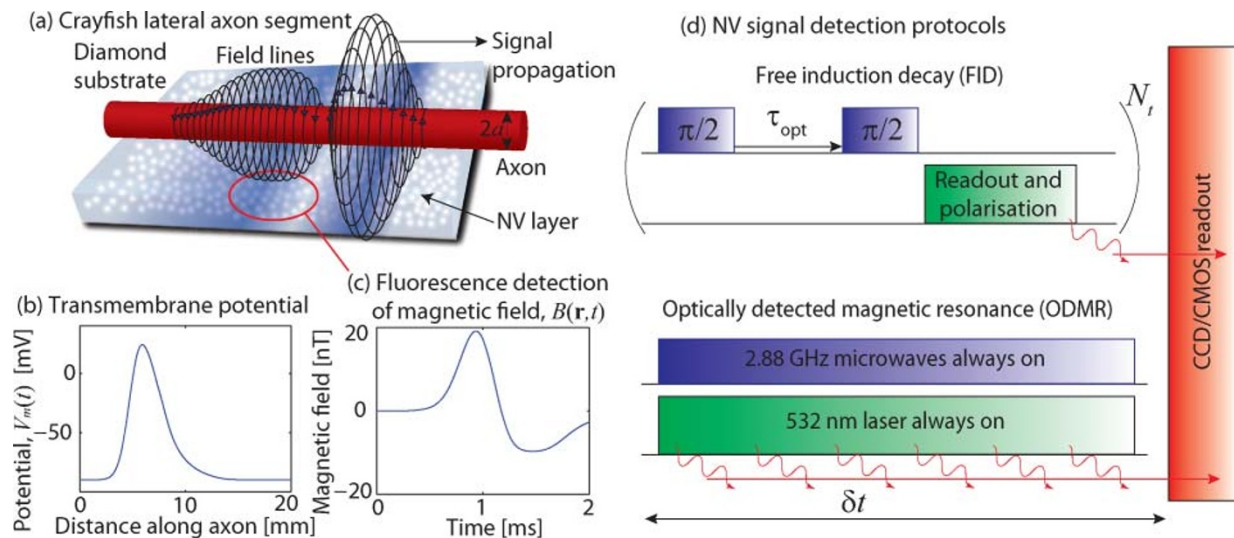


Figure 2 | (a) Schematic of the NV-diamond neuron detection system showing a neural network component (in this case an axon) on a diamond substrate containing fluorescent NV centres. For a FID based protocol, regions where the field is greatest produce the least fluorescence. For an ODMR based protocol, the converse is true. (b) Longitudinal variation of the transmembrane potential, V_m , of a crayfish lateral axon as taken from Ref.²¹. As this excitation propagates along the axon, it produces a time dependent magnetic field like that shown in (c) for a standoff of 100 nm. (d) Temporal arrangement of microwave and optical pulse sequences. For the FID based protocol, $\pi/2$ microwave pulses are used to prepare the NV in a superposition of $|0\rangle$ and $|1\rangle$ states which accumulate a relative phase shift during the free evolution period due to the presence of a neural field. A second $\pi/2$ pulse transforms this phase into a population difference which is read out using a 532 nm laser. Application of this laser also acts to re-polarise the NV in the $|0\rangle$ state. The decreased intensity of the collected fluorescence permits the determination of the phase shift and hence the strength of the neural magnetic field. In the case of an ODMR based protocol, the constantly applied microwaves drive transitions between the paramagnetic sublevels of the ground states, whose relative energies are altered by the presence of a neural field, making the $|0\rangle \rightarrow |1\rangle$ transition less likely, resulting in an increased fluorescence.

to obtain the resulting magnetic fields, $B(r, t)$. In Fig. 2 we show this for the case of a crayfish lateral axon using the measured transmembrane potential [Fig. 2(b)] taken from Ref.²¹. The resulting magnetic field signal calculated at the NV position is shown in Fig. 2(c) for a 100 nm standoff. Typically, the magnetic fields generated by the transmembrane potential are at the nT scale. We will show that the quantum detection system based on optically detected magnetic resonance (ODMR) of the NV centre in diamond has the combination of sensitivity and the appropriate spatial scale to enable detection of the neuronal magnetic fields at the high temporal-spatial resolution required.

Theoretical proposals for the use of NV centres as sensitive, single spin magnetometers^{22,23} have been followed by proof-of-principle experiments^{11,12,24}. Despite their promise, biological systems are generally of a stochastic nature and are not always compatible with protocols designed to sense highly controllable DC and AC signals. It was recently shown that decoherence microscopy methods²⁵ permit the characterisation of randomly fluctuating magnetic fields²⁶. Methods to characterise random AC fields of random frequency and phase have also been proposed²⁷. In addition to their use as fluorescent biomarkers^{16,28–31}, NV centres have recently received much attention as sensors of magnetic biological processes, in particular as sensors of ionic flux through single ion channels in lipid membranes³², and intra-cellular micro-fluid dynamics¹⁴. The advent of widefield NV magnetometry based on CCD detection of a high NV density diamond substrate has yielded the ability to spatially reconstruct magnetic fields at the μm scale together with improved sensitivity over that obtainable with a single NV centre whilst retaining the necessary quantum coherence properties³³. Further improvements are expected in the near future, with nitrogen to NV⁻ conversion efficiencies in excess of 50% having been recently reported^{34,35}.

We envisage two detection protocols based on either directly monitoring the coherent phase difference between the sublevels of the NV centre using free induction decay (FID) experiment; or by measuring the location of the resonance peak in a continuous wave ODMR

experiment [Fig. 2(d)]. The sensitivities of the two methods are essentially equivalent²⁴, however for definiteness (and brevity) we describe in more detail the former. At fiducial $\tau = 0$, following optical polarisation into the $m_s = 0$ state, the application of a $\pi/2$ microwave pulse places each NV centre into an even superposition of $m_s = 0$ and $m_s = 1$ Zeeman levels. After a free evolution time of τ , another $\pi/2$ pulse is applied and the system's state is read out optically. In the absence of any magnetic disturbances the system remains coherent, and the probability of finding the NV system in the $m_s = 0$ magnetic level after the second $\pi/2$ pulse, measured directly from its fluorescence, will oscillate between 0 and 1 at a frequency given by the energy difference of the two levels. However, in reality such coherent superpositions of quantum states are highly sensitive to magnetic field fluctuations in the immediate crystalline environment due to mutual spin flipping of electronic nitrogen defects and/or ¹³C nuclear spins. Thus, depending on the material composition, one typically measures a decay of these coherent oscillations between the magnetic levels as a function of the evolution time τ . For isotopically pure diamond the timescale of this decoherence, referred to as the FID time T_2^* , is typically of order 1 to 10 μs and ultimately sets the sensitivity limits for an NV based magnetometer. By employing a spin-echo pulse sequence in which an additional π -pulse is applied at time $\tau/2$, coherence times may be extended by more than 2 orders of magnitude, and further improvements may be realised by employing higher order decoupling schemes such as CPMG^{23,36} or Uhrig^{37,38} pulse sequences. Such decoupling schemes achieve improvements to the sensitivity by suppressing the effect of low frequency noise on the NV centre, and are hence not suited to measuring neural magnetic fields which fluctuate on $T = 1$ to 10 ms timescales. To ensure maximal sensitivity to low frequency noise we must employ some N_t repetitions of the FID or ODMR protocols in the time interval $[t, t + \delta t]$. As such, δt serves to define the temporal resolution of the system, and must satisfy $\delta t < T$. Furthermore, each protocol cycle must be sufficiently sensitive that $N_t \lesssim T/T_2^*$ measurements may be taken within the timescales associated with the



neuronal dynamics, whilst maintaining an acceptable signal to noise ratio (SNR).

During its evolution under the neural magnetic field $B(\mathbf{r}, t)$, the coherent phase accumulation is of an NV centre at position \mathbf{r}_i during time interval τ , is given by $\Delta\phi(\mathbf{r}_i) = \gamma \int_0^\tau B_i(\mathbf{r}_i, t) dt$, where γ is the NV gyromagnetic ratio and B_i is the component of \mathbf{B} parallel to the i^{th} N-V axis. The signal change we are interested in measuring is the resulting change in fluorescence due to this phase accumulation, which is proportional to $\sin(\Delta\phi)$. Since the neural magnetic fields considered here are typically less than 10 nT, and are essentially constant over the timescale of a single measurement protocol, we have that $\Delta\phi \ll 1$, thus the signal change at a single defect site is given by $S_i \approx \gamma \tau B_i(\mathbf{r}_i) D(\mathbf{r}_i, \tau)$, where $D(\mathbf{r}_i, \tau)$ is the decoherence envelope of the NV defect at position \mathbf{r}_i as a function of the interrogation time, τ . This envelope represents the decay of quantum coherence of defect i due to interactions with the surrounding magnetic environment, including ^{13}C nuclei, nitrogen electron spins, and other proximal NV centres. As we are considering an FID sequence, the shape of each envelope is assumed to be Gaussian, and is given by

$$D(\tau) = \exp \left[- \left(\Gamma_{\text{c13}}^i \tau \right)^2 - \left(\Gamma_n^i \tau \right)^2 \right], \quad (2)$$

where $\Gamma^i \equiv \Gamma(\mathbf{r}_i)$ is the intrinsic decoherence rate of NV centre i , and $\Gamma_{\text{c13}} \sim 100$ kHz. The decoherence rate due to nitrogen impurities, Γ_n will explicitly depend on the nitrogen density and must be optimised, as shown below. The total signal from a single FID protocol cycle, $S = \sum_i S_i$, is the sum of the signals from all NV centres, and in the high NV density limit, is given by

$$S(\tau) = \alpha \gamma \tau n \int_{V_p} B_i(\mathbf{r}, \tau) D(\mathbf{r}, \tau) d^3 \mathbf{r}, \quad (3)$$

where n is the total electron spin density due to both nitrogen and NV defect centres (assumed uniform for chemical vapor deposition grown samples, and an axially-symmetric Gaussian for implanted samples), α is the nitrogen-NV conversion efficiency, and V_p is the volume of a given pixel. Since the measurement of each NV centres is projective, the total signal distribution follows the central limit theorem and the uncertainty in the signal is given by

$$\delta S = \frac{1}{C} \sqrt{\frac{N_p}{N_t}}, \quad (4)$$

where C is an experimental parameter accounting for imperfect photon collection (including non-unity quantum efficiency of the detector) and signal contrast, and N_p is the effective number of NV defects (probes) in V_p , given by $N_p \approx \alpha n V_p$. To measure the magnetic field of an axon, ultimately we require $S \gtrsim \delta S$.

We now consider a simple, analytically solvable case where the axon dimensions are large ($\sim 60 \mu\text{m}$, as in the case of a crayfish lateral axon²¹) compared with a sensing volume of $V_p \sim (1 \mu\text{m})^3$, ensuring there is little variation in the magnetic field strength over the sensing volume (i.e. $B_i \equiv B \forall i$). The signal is then $S \approx \alpha n V_p \gamma B \tau$. The minimum detectable magnetic field is then

$$\delta B = \frac{1}{\gamma C \sqrt{\alpha N_t V_p}} \frac{\exp \left[\tau^2 \left(\Gamma_{\text{c13}}^2 + \Gamma_n^2 \right) \right]}{t \sqrt{n}}, \quad (5)$$

which we wish to optimise for n and τ , giving firstly $\tau_{\text{opt}} = \left(2\Gamma_{\text{c13}}^2 + 2\Gamma_n^2 \right)^{-1/2}$. The dephasing due to nitrogen is given

by $\Gamma_n = \kappa n^{38}$, where $\kappa = \sqrt{\frac{\pi}{3}} \frac{\mu_0}{4\pi} \hbar \gamma^2$. Setting $\frac{\partial}{\partial n} \delta B = 0$ gives $\Gamma_{\text{c13}} = \Gamma_n$, hence $n = \Gamma_{\text{c13}} / \kappa = 2.3 \times 10^{23} \text{m}^{-3} = 1.3 \text{ppm}$, an order of magnitude below the maximum reported density achieved in practice to date of $2.8 \times 10^{24} \text{m}^{-3}$ ³⁹. The minimum detectable field by a pixel of volume V_p is then

$$\delta B = \frac{3.3 \text{ nT } \mu\text{m}^{3/2}}{C \sqrt{\alpha N_t V_p}}.$$

For example, an implementation with $C = 0.3$ and an N-NV conversion ratio of $\alpha = 0.1$ would be capable of resolving a magnetic field to an accuracy of 3.5 nT in an integration time of 1 ms ($N_t = 100$).

In the large axon case considered here, increasing V_p will result in an improved sensitivity, however this will not be true in general. As V_p becomes comparable to the axon dimensions, the field felt by distant NV centres will be significantly less than that felt by those proximate to the axon, and the integral in Eq. 3 will no longer scale linearly with V_p . The noise amplitude however [Eq.4] will grow with the square root of the sensing volume, regardless of the axon field characteristics. If the sensing volume is sufficiently large that the signal exhibits sub-square root scaling with the sensing volume, there will be no advantage in having a larger V_p . As such, better results for smaller neural components will be achieved by optimising the V_p for the task at hand.

The maximum frequency with which measurements may be taken is $f_m = (\tau_{\text{opt}} + \tau_m)^{-1}$, where $\tau_{\text{opt}} = (2\Gamma_n)^{-1}$ from above, and $\tau_m \sim 350$ ns is the time required for photon collection and subsequent repolarisation of the NV spin state. To gain further improvements to the SNR, we envisage taking numerous measurements with frequency f_m , and applying a low-pass filter to the measurement record. Incorporating a greater number of timepoints in this process will improve the sensitivity, however this comes at a cost of decreased temporal resolution, $\delta t = N_t / f_m$. A faithful reconstruction of the field dynamics with time-lag δt will be possible provided δt is less than the characteristic timescales of the neural dynamics.

$$\delta t = \left(\frac{3.3 \text{ nT}}{B} \right)^2 \frac{\tau_{\text{opt}} + \tau_m}{C \sqrt{\alpha V_p} \mu\text{m}^{3/2}}. \quad (6)$$

The effect of averaging over different ranges of measurements and the trade-off that exists between a high SNR and high temporal and spatial resolution is considered later for the case of the Hippocampal CA1 pyramidal neuron.

Comparison of magnetic and electric field detection. This method of monitoring neuron function through the magnetic fields generated offers a distinct advantage over consideration of the resulting electric fields. The electric field is a consequence of the local gradient of the electric potential, whereas magnetic field detection is sensitive to non-local field sources. That is, the external magnetic field is a consequence of both the internal and external electric fields, the strength of the former being some 3 orders of magnitude larger than the latter.

Electric field detection protocols using single electron transistors (SETs) have sensitivities of $2 \text{ V cm}^{-1} \text{ Hz}^{-1/2}$ at standoffs of 100 nm^{41} , however there are significant practical compatibility issues associated with real neural samples and the need for cryogenic sensing operation. Electric field sensing using NV centres does allow for room temperature operation, however the associated DC field sensitivity was recently demonstrated at $613 \text{ V cm}^{-1} \text{ Hz}^{-1/2}$ ⁴², whereas single NV sensitivities to DC magnetic fields have been demonstrated at $43 \text{ nT Hz}^{-1/2}$ ⁴⁰. The peak magnitudes of magnetic and electric fields around a typical axon are shown in Fig. 3(a), yielding 3 nT and $40 \times 10^{-3} \text{ V cm}^{-1}$, respectively, at a standoff of 100 nm . For the sake of comparison, Fig. 3(b) shows the time required for a single NV centre to resolve the magnetic and electric field strengths in the region surrounding a typical axon. Clearly local magnetic detection offers an advantage in terms of both spatial and temporal resolution.

Experimental verification of detection protocol. To experimentally demonstrate the effectiveness of the proposed detection protocol for neuron specific signals, and quantitatively verify the theoretical analysis, we replicated the magnetic field produced by a single

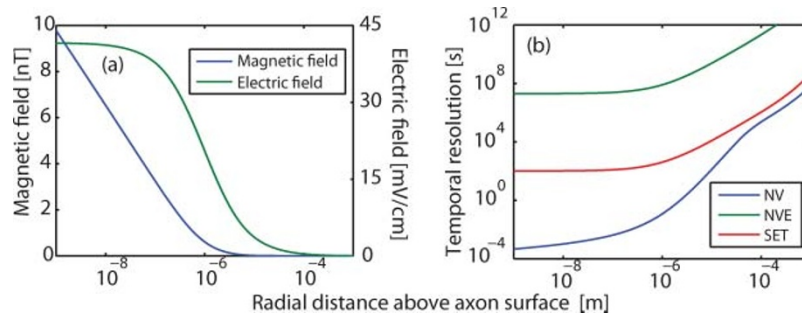


Figure 3 | (a) Dependence of magnetic and electric field strength on radial distance above the axon surface. The more immediate attenuation of the magnetic field permits roughly an order of magnitude better spatial imaging resolution as compared with the electric field. Note the different axes used for electric and magnetic fields. (b) Comparison of the temporal resolution corresponding to sensing the magnetic field using diamond crystal containing a high NV centre density (NV, blue), and sensing the electric field using the same NV centre density (NVE, green) and a single electron transistor (SET, red).

axon using a microwire on the surface of a diamond substrate [Fig. 4(a)]. The pulses were constructed such that the resulting Biot-Savart field emulates the temporal dynamics of the axon considered in the preceding section [Fig. 4(b)]. A single NV centre, located at a lateral distance of approximately 10 μm from the wire, was used as the sensor (see Methods section).

We simulated the detection gain of N_p centres by repeating the measurement process N_s times. The binning widths for the photon integration times were $t_p = 24.2 \mu\text{s}$, and the total time taken to send two successive pulses down the wire was 20 ms [Fig 4(d)]. The dynamics of this signal place a limit on the permissible temporal resolution, $\delta t \approx 1 - 2$ ms, hence the maximum number of data points employed in the low-pass filtering process is $N_t = \delta t/t_p \approx 50$. Assuming a constant sensitivity, the effective number of centres involved in the detection may then be determined from

$N_p = \frac{N_s}{N_t} \left(\frac{B_w}{B_a} \right)^2$, where B_w is the peak magnetic field strength due to the pulse in the wire, and B_a is the peak magnetic field strength due to the axon. This assumption was experimentally verified by measuring the minimum detectable magnetic field for a range of photon integration times [Fig 4(c)], from which a corresponding sensitivity of $10 \mu\text{T Hz}^{-1/2}$ was determined [Fig 4(d)], for this (non-optimised) system.

The figures of merit are the effective spatial and temporal resolutions, given by $\delta x = (N_p/n)^{1/3}$ and $\delta t = N_t t_p$ respectively. The measurement record obtained by monitoring a pulse with $B_w = 24 \mu\text{T}$, and $N_s = 5,000$ cycles is given by the green trace in Fig 4(b). From the above scaling, this is equivalent to a pixel volume of $V_p = (7.9 \mu\text{m})^3$ at a temporal resolution of $\delta t = 1.3$ ms. Sacrifices in the temporal resolution will allow for decreases in the required pixel volume, for

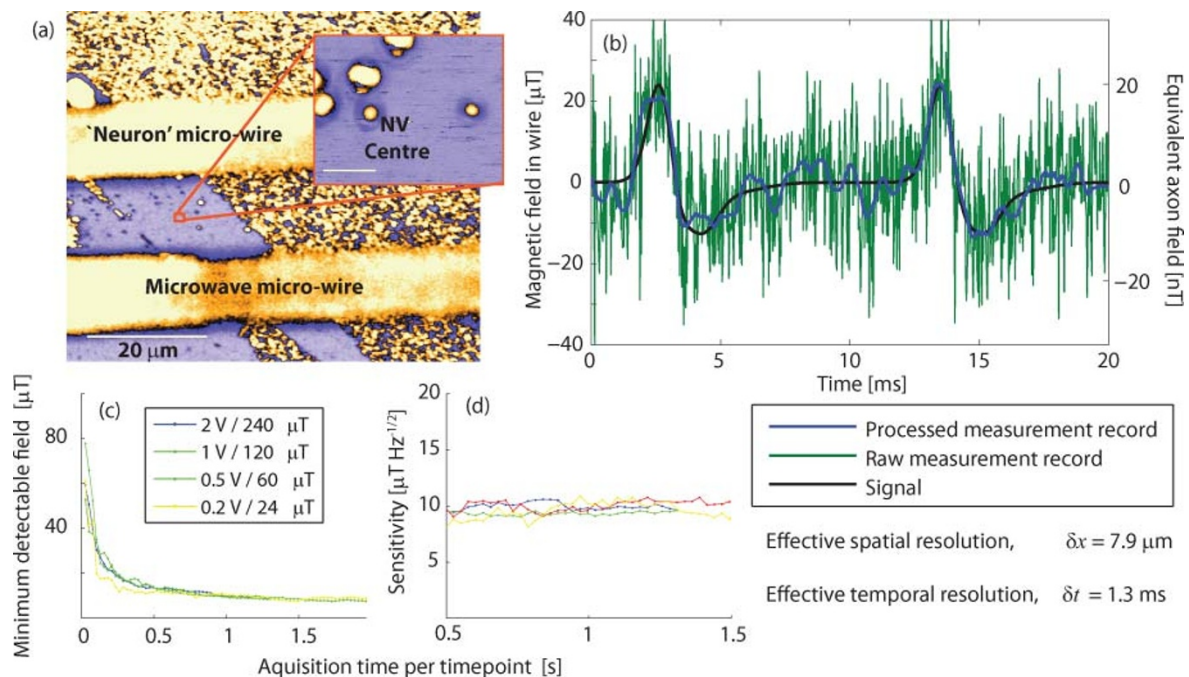


Figure 4 | Detection of experimentally simulated neuron signals using the ODMR detection protocol on a single NV centre. (a) Confocal fluorescence image showing the spatial arrangement of the NV with respect to the microwave and artificial neuron signal micro-wires. (b) Experimental measurement of the electronically generated neuron pulse together with the extrapolated effective spatial and temporal resolution corresponding to a high NV density widefield detection system. Optimisation of this protocol to achieve higher resolutions is discussed in the main text. (c) Experimental minimum detectable magnetic field, δB vs total photon integration time, T , showing a $\delta B \propto T^{-1/2}$ dependence. This dependence is verified by plotting the corresponding sensitivity, $\eta = \delta B\sqrt{T}$, in (d), showing the sensitivity is effectively constant.



example, a pixel volume of $V_p = (1 \mu\text{m})^3$ has a corresponding temporal resolution of $\delta t = 2 \text{ ms}$. These figures clearly demonstrate, experimentally, that NV centres are capable of simultaneously resolving both the spatial structure and temporal dynamics of neuronal magnetic fields, even in their current, unoptimised implementation. Further improvements may be achieved with the use of higher grades of isotopically pure diamond crystal, as used in⁴⁰, where single-spin DC magnetic field sensitivities of $43 \text{ nT Hz}^{-1/2}$ were demonstrated. Extrapolating this to the present context, such sensitivities would permit a pixel volume of $V_p = (0.2 \mu\text{m})^3$ at a temporal resolution of 1.3 ms . How these capabilities relate to the spatial and temporal characteristics of a biological neuronal network are discussed in the following section.

Imaging simulation: the hippocampal CA1 pyramidal neuron. In order to quantitatively describe how the device would sense and image neural activity we simulated the magnetic fields that would be produced by a neuron while it receives synaptic input and generates and fires an action potential output. The neuron model we used was of a morphologically reconstructed hippocampal CA1 pyramidal neuron. Hippocampal CA1 pyramidal neurons have an extended morphology, show a rich repertoire of dynamics and are involved in networks that underlie important behaviour such as learning and memory. Study of these neurons and the networks they reside in will be a major target of the techniques described here.

Typically such an experiment would be performed in vitro using a buffer solution of phosphate buffered saline (PBS), or equivalent. Such solutions contain dissolved sodium and potassium salts at concentrations of roughly 150 mmol L^{-1} , giving rise to nuclear spin concentrations of roughly 10^{25} m^{-3} , some 5 orders of magnitude less than the hydrogen nuclear spin concentration due to water molecules. The hydrogen spins themselves produce an effective stochastic magnetic field with fluctuations caused by molecular self-diffusion. This would cause the decoherence rates of NV centres at even a few nanometres from the diamond surface to increase by approximately $100 \text{ Hz}^{-1} \text{ kHz}^{32}$, some 2–3 orders of magnitude less than that due to intrinsic decoherence sources, and can therefore be ignored.

The model consists of 265 anatomical sections [Fig. 5(a)] and 15 voltage and calcium activated conductances with a non-uniform distribution across the morphology. We stimulated the model neuron with 2 nA current injections into 21 sites on distal dendrites. The associated transmembrane potentials at specific locations are shown in Fig. 5(b). As the distal dendrites are stimulated current flows along these processes towards the soma. The associated magnetic field strength changes are readily seen in the sequence of time snapshots, Fig. 5(c–e). As the membrane potential increases the soma current flow along the dendrites decreases, reducing the magnetic field strength [Fig. 5(c)]. As active conductances in the soma and axon are recruited, current flow increases in these compartments and the

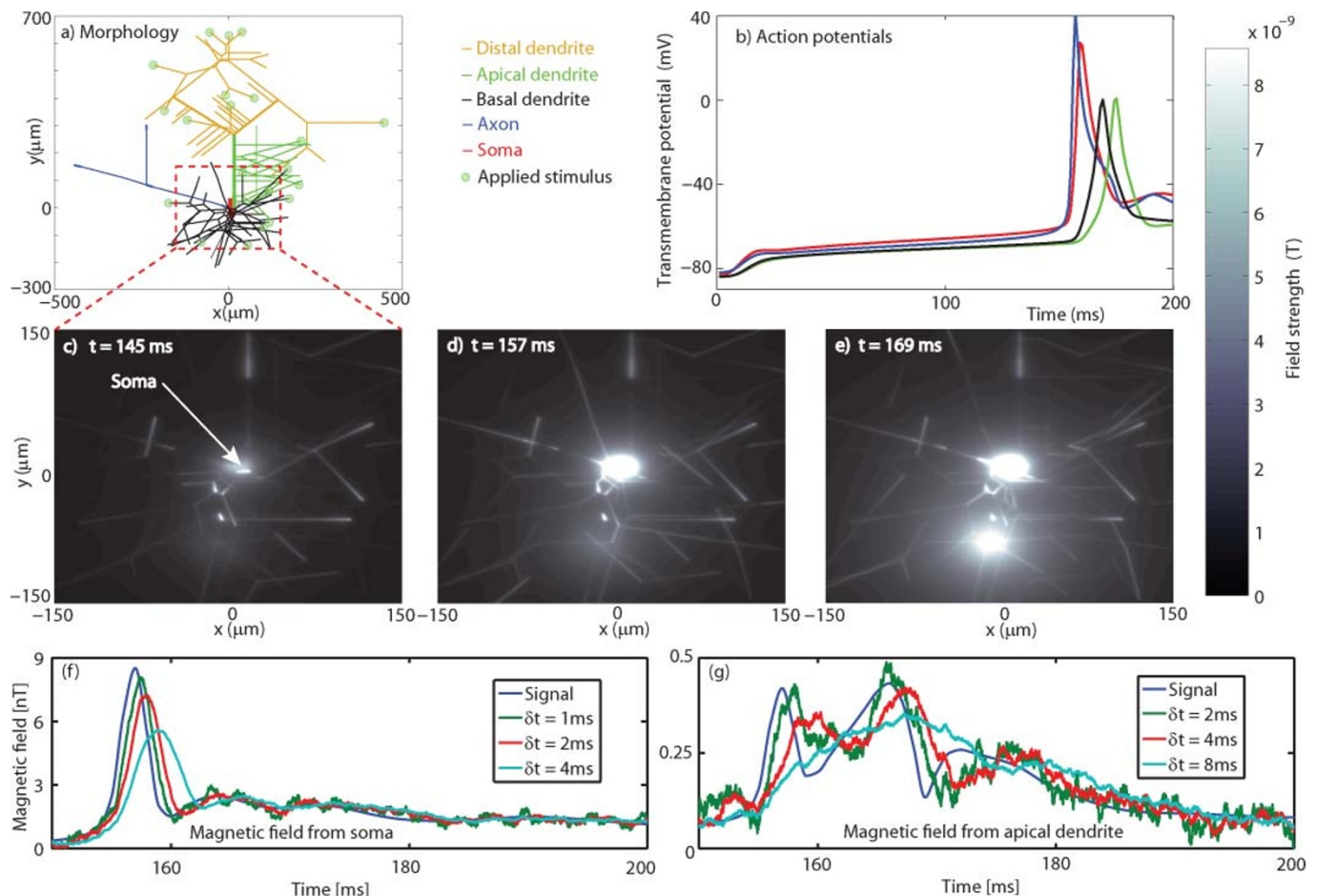


Figure 5 | (a) Morphology of the Royeck-Wimmer model and input excitation sites. (b) Transmembrane potentials generated at the soma, axon and dendrites shown in (a). (c–e) Zoomed plots of magnetic field strength at 100 nm standoff showing the integrate and fire effect of the central soma and the reactionary dynamics in the dendritic region below. Simulated measurements taken at (f) $0 \mu\text{m}$ and (g) $45 \mu\text{m}$ along the apical dendrite directly above the soma, as shown in (a) for a detection volume of $V_p = (2 \mu\text{m})^3$ and a range of integration times, δt . Note the change of magnetic field strength scale in (f) and (g), resulting in the latter requiring longer integration times. Assumed parameter values are $C = 0.05$, and $\alpha = 0.1$.



field strength increases. Eventually an action potential is triggered in the soma and distal axon [Fig. 5(d)]. The initiation point in the distal axon is not as bright as the soma because the technique is sensitive to longitudinal currents, not voltage. A back propagating action potential is also triggered in the basal dendritic tree [Fig. 5(e)].

In Fig. 5(f)&(g) we show the single ($2\ \mu\text{m}$) pixel detection trace of the neuronal magnetic field at two locations below the neuron structure in response to the applied stimuli, assuming experimentally realised values of $C = 0.05^{43}$, and $\alpha = 0.1$. The magnetic field signal is plotted together with the simulated measurement output for a range of integration times, δt . As the integration time is increased the SNR improves, at the cost of temporal resolution in the neuronal signal itself. However, it is evident that a minimal time-lag of 1 ms gives an acceptable account of the neuron signal in all three cases.

Finally, we determine the overall spatial-temporal resolution of the imaging system by explicitly considering the trade-off between integration time and detection volume. In Fig. 6 we show the simulated CMOS/CCD output (assuming a readout rate of 500 fps, as available with current technology²⁰) for a snap-shot of the neuron activity at $t = 157\ \text{ms}$ for a range of integration times δt and spatial detection volumes δx . It is clear that the neuronal magnetic field structure is apparent at $[\delta x, \delta t] = [2\ \mu\text{m}, 1\ \text{ms}]$, showing the imaging system has the temporal resolution to fully map the magnetic field dynamics of a neuronal network, whilst

simultaneously reproducing the structural morphology at the sub-cellular level.

Discussion

We have investigated the use of the magnetic field sensing properties of NV-ensembles in diamond for imaging neural activity. Using published crayfish lateral axon biophysical data we determined the magnetic field signal at 100 nm from the axon surface to demonstrate that it lies within the sensitivity range of our detection system. The sensitivity regime for detection of the magnetic field dynamics generated in the axon structure was determined based on both pulsed (FID) and continuous wave (ODMR) sequences. Direct measurement of axon-scale magnetic fields, produced by passing current in a proximate microwire, verified that the sensitivity limits fell within the range needed to detect neuronal signals. To explore the potential utility of NV arrays as wide field detectors of neuronal network activity we simulated the three dimensional magnetic fields associated with action potential propagation in a morphologically realistic hippocampal CA1 pyramidal neuron placed 100 nm from the NV detection layer. The simulated photon emission of our model neuron/NV-layer combination was projected onto a virtual CMOS array to investigate the performance of the sensor in detecting local and wide-field neuronal structure and dynamics. By exploring different combinations of integration times, δt , and

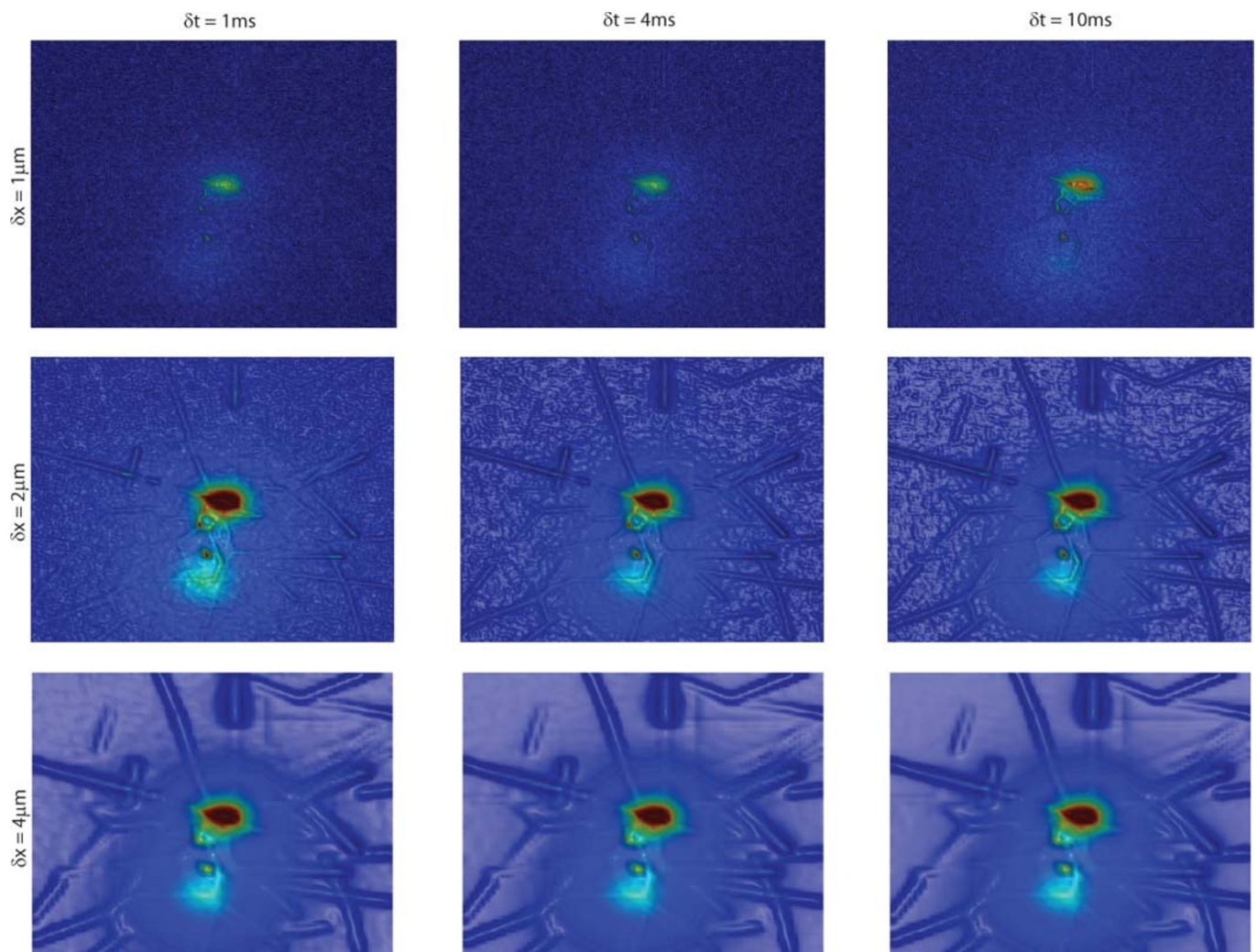


Figure 6 | Simulated snapshot of the CCD output at $t = 157\ \text{ms}$ and for a range of detection volumes, $V_p = (\delta x)^3$ and integration times δt . Assumed parameter values are $C = 0.05$, and $\alpha = 0.1$.



detection regions, δx , we found that the performance of the sensor enabled simultaneously high temporal and spatial resolution of extracellular field potentials in regimes beyond those obtained by current methodologies. In summary, our experimental results and theoretical work establish the significant potential of this quantum based technique to visualise the key components of neuronal network activity, subthreshold signalling, action potential initiation and propagation in axons, soma and dendritic compartments, at relevant scales to provide new views into network function. To bring this imaging concept to reality one must assemble all the individual and non-trivial components, such as sufficiently dense near-surface NV layer structures in high grade diamond material, neuron growth on these diamond surfaces, and microwave quantum control and optical wide-field readout commensurate with long term integrity and function of the biological structure. Precursor experiments based on well characterized biological systems will extend the experimental work carried out here on model neuronal signals.

Methods

Optically detected magnetic resonance (ODMR). ODMR detection is based on monitoring the NV fluorescence spectrum in response to an applied oscillating microwave field. The constantly applied microwaves drive transitions between the paramagnetic sublevels of the ground states, whose relative energies are altered by the presence of a background field. The effect of the field, B , will be to shift the frequency spectrum, $S(\omega)$, by an amount γB to give $\tilde{S}(\omega) = S(\omega - \gamma B)$. At some chosen reference point in the spectrum there will be a corresponding change in the number of photon counts proportional to $\Delta N(\omega) \propto \Delta S(\omega) = S(\omega) - \tilde{S}(\omega)$. For small fields, this change will depend on the local gradient of the spectrum, $\Delta S \approx \frac{d}{d\omega} S(\omega) \Delta\omega = \gamma B \frac{d}{d\omega} S(\omega) \equiv \kappa \gamma B$.

The spectrum is given by a Lorentzian distribution of Full Width Half Maximum Γ , centred about γB_0 ,

$$S(\omega) = N_0 \left(1 - \frac{C\Gamma^2}{\Gamma^2 + \gamma^2(B - B_0)^2} \right), \quad (7)$$

where N_0 is the unperturbed photon count in regions of the spectrum far detuned from resonance and C , is the difference in photon counts between the resonant and unperturbed regions. The maximum gradient occurs at $\omega = \pm \gamma B_0 \pm \Gamma/\sqrt{3}$, giving

$$k = \max \left\{ \frac{d}{d\omega} S(\omega) \right\} = CN_0 \frac{3\sqrt{3}}{8\Gamma}. \quad (8)$$

To ensure a signal to noise ratio of greater than 1, we require $\Delta S > 1/\sqrt{N} = 1/\sqrt{Rt}$, where N is the total number of photons collected in time t , and R is the photon count rate. Hence the minimum detectable field strength and corresponding sensitivity are

$$B_{\min} = \frac{1}{C\gamma\sqrt{Rt}} \frac{8\Gamma}{3\sqrt{3}}, \quad (9)$$

$$\eta = \frac{1}{C\gamma\sqrt{R}} \frac{8\Gamma}{3\sqrt{3}}. \quad (10)$$

The countrate, R , is a monotonically increasing function of the laser power that saturates at approximately 140 kHz, and both C and Γ are functions of the microwave and laser power. Maximal sensitivity will be achieved by optimising these parameters to reach the operating regime of the ODMR protocol that yields the maximum value of k .

Calculation of the magnetic field from a transmembrane potential. Numerical simulations of the transmembrane potentials of the Rocyte model were performed using the NEURON software package. Given an arbitrary form for the transmembrane potential along a given component of the neural network, we may use the corresponding Fourier transform, $\mathcal{F}[V_m(z, t)]$, with respect to the longitudinal coordinate z and conjugate variable k to compute the electric potentials inside and outside of the component.

$$\Phi_i(r, z, t) = \frac{\sigma_i}{2\pi} \mathcal{F}^{-1} \left[\mathcal{F}[V_m] \frac{I_0(|k|r)K_1(|k|a)}{G(|k|a)} \right],$$

$$\Phi_o(r, z, t) = -\frac{\sigma_o}{2\pi} \mathcal{F}^{-1} \left[\mathcal{F}[V_m] \frac{K_0(|k|r)I_1(|k|a)}{G(|k|a)} \right],$$

where σ_i and σ_o are the conductivities of the interior and exterior regions respectively, and I_n and K_n are the n^{th} order modified Bessel functions of the first and second kind respectively, \mathcal{F}^{-1} denotes the inverse Fourier transform, and $G \equiv \sigma_o K_1 I_0 + \sigma_i K_0 I_1$. Current densities may be found from Ohm's law, $j^i = \sigma_i \nabla \Phi^i$. For the cases considered here, the longitudinal current density is approximately 2 orders of magnitude larger than that in the radial direction, which we consequently ignore. The longitudinal current densities are given by

$$\tilde{j}_i^z(r, z, t) = \frac{\sigma_i \sigma_o}{2\pi i} \mathcal{F}^{-1} \left[k \mathcal{F}[V_m] \frac{I_0(|k|r)K_1(|k|a)}{G(|k|a)} \right],$$

$$\tilde{j}_o^z(r, z, t) = -\frac{\sigma_i \sigma_o}{2\pi i} \mathcal{F}^{-1} \left[k \mathcal{F}[V_m] \frac{K_0(|k|r)I_1(|k|a)}{G(|k|a)} \right],$$

The magnetic fields due to the current densities may be evaluated using the Biot-Savart law,

$$\mathbf{B}(\mathbf{r}) = \frac{\mu_0}{4\pi} \int \frac{\mathbf{J}(\mathbf{r}') \times (\mathbf{r} - \mathbf{r}')}{|\mathbf{r} - \mathbf{r}'|^3} d^3\mathbf{r}',$$

$$B_\phi(\mathbf{r}) = \frac{\mu_0}{2\pi} \sqrt{\frac{a}{r}} \int_{-\infty}^{\infty} [j_i^z(a_-, z') - j_o^z(a_+, z')] \times \frac{(1 - \chi^2)K(\chi^2) - 2E(\chi^2)}{\chi} dz',$$

where B_ϕ is the azimuthal component of the field, and $K(\chi^2)$ and $E(\chi^2)$ are the elliptical integrals of the first and second kind respectively given by

$$K(\chi^2) = \int_0^{2\pi} [1 - \chi^2 \sin^2(\alpha)]^{-1/2} d\alpha$$

$$E(\chi^2) = \int_0^{2\pi} [1 - \chi^2 \sin^2(\alpha)]^{1/2} d\alpha$$

$$\text{and } \chi^2 \equiv \frac{4ar}{(a+r)^2 + (z-z')^2},$$

$$\alpha \equiv \frac{1}{2}(\theta' - \pi).$$

Experimental verification of ODMR based measurement protocol. Following²¹, we fit the transmembrane potential using a sum of three Gaussian curves,

$$V_m = V_0 \sum_i A_i \exp[-B_i^2(t - C_i)^2],$$

hence the external magnetic field near the membrane will be proportional to

$$\frac{dV_m}{dt} = -2V_0 \sum_i B_i^2(t - C_i) A_i \exp[-B_i^2(t - C_i)^2].$$

The experiment was performed by using an arbitrary waveform generator to propagate two sequential pulses of this shape along a 10 μm wire. The resulting magnetic field was measured by the change in fluorescence of an NV centre separated from the wire by a lateral distance of approximately 10 μm . The dependence of the magnetic field strength on the signal voltage was determined by driving DC signals in the wire and monitoring the peak splitting of the NV ODMR spectrum. From this, we determined the NV centre experiences a magnetic field of 120 nT for every mV applied to the wire. This corresponds to 360 nT for every mA of current in the wire due to an electrical resistance of 3 Ω .

Since the magnetic field is proportional to the applied voltage, we use the following fit for the NV fluorescence

$$S = S_0 - \sum_{j=1}^2 \sum_{i=1}^3 S_j A_i B_i^2 \left(\frac{t - t_j}{\tau_j} - C_i \right) \times \exp \left[-B_i^2 \left(\frac{t - t_j}{\tau_j} - C_i \right)^2 \right], \quad (11)$$

where S_j , t_j and τ_j are the relative amplitude, offset and dilation of the j^{th} pulse, and A_i , B_i and C_i are as above. An example of the fit to a pulse with peak voltage of 200 mV is shown in Fig. 4(b). Each timepoint represents a photon integration time of 24.2 μs . The effect of increasing the number of NV centres involved in the detection is simulated by varying the number of cycles per time point from 1,000 to 50,000.

From this fit, we may determine the mean square error, which gives the uncertainty in the photon counts, δN . The maximum signal contrast, ΔN is given by the difference between the maximum value of the fitted function, $\max(S)$ and the value that represents 0 magnetic field, S_0 . That is, $\Delta N = \max(S) - S_0$. The uncertainty in the magnetic field strength is defined such that the magnetic field measurement has the same signal to noise ratio as that of the photon counts,

$$\text{SNR} = \frac{\Delta B}{\delta B} = \frac{\Delta N}{\delta N}.$$

Since we know the peak magnetic field is 120 nT per mV of signal in the microwire, we may determine the corresponding uncertainty in the magnetic field, which in turn defines the minimum detectable magnetic field,

$$\delta B = \Delta B \frac{\delta N}{\Delta N} \\ = \Delta B \frac{\delta N}{\max(S) - S_0}.$$



Summary of physical and detection timescales.

Typical neuronal pulse duration	$\delta t = 2$ ms
NV spin dephasing time	$T_2^* = 1/\Gamma = 10 \mu\text{s}$
Peak neuronal magnetic field value at 100 nm from axon surface	$B = 10$ nT
Single NV centre sensitivity	$\eta_0 = 10 \mu\text{T Hz}^{-1/2}$ (43 nT $\text{Hz}^{-1/2}$ for isotopically pure crystals ⁴⁰)
High density NV centre sensitivity	$\eta = 2 \times 10^{-3} \mu\text{m}^{3/2} \times \eta_0 / \sqrt{V_p}$
Maximum CMOS/CCD framerate	530 fps

The total acquisition/integration time for each data point is the product of the binning time, $\Delta t = 24.2 \mu\text{s}$, and the number of cycles, N_p . Hence we may plot the minimum detectable field, δB , against the integration time, $T = N_p \Delta t$, as shown in Fig. 4(c). The sensitivity is defined by $\eta = \delta B \sqrt{T}$ and is plotted in Fig. 4(d), which is effectively constant.

- Cohen, M. R. & Kohn, A. Measuring and interpreting neuronal correlations. *Nat. Neurosci.* **14**, 811–819 (2011).
- Grillner, S., Markram, H., De Schutter, E., Silberberg, G. & LeBeau, F. E. N. Microcircuits in action - from cpgs to neocortex. *Trends Neurosci.* **28**, 525–533 (2005).
- Fenno, L., Yizhar, O. & Deisseroth, K. *Annu. Rev. Neurosci.* **34**, 389–412 (2011).
- Baker, B. J. *et al.* Imaging brain activity with voltage- and calcium-sensitive dyes. *Cell. Molec. Neurobiol.* **25**, 245–282 (2005).
- Homma, R. *et al.* Wide-field and two-photon imaging of brain activity with voltage- and calcium-sensitive dyes. *Philos. Trans. R. Soc. Lond. B* **364**, 2453–2467 (2009).
- Perron, A. *et al.* Second and third generation voltage-sensitive fluorescent proteins for monitoring membrane potential. *Front. Mol. Neurosci.* **2** (2009).
- Qing, Q. *et al.* Nanowire transistor arrays for mapping neural circuits in acute brain slices. *Proc. Natl. Acad. Sci. USA* **107**, 1882–1887 (2010).
- Duan, X. *et al.* Intracellular recordings of action potentials by an extracellular nanoscale field-effect transistor. *Nature Nanotechnology* **7**, 174–179 (2012).
- Robinson, J. T., Jorgolli, M., Shalek, A. K., Yoon, M. H., Gertner, R. S. & Park, H. Vertical nanowire electrode arrays as a scalable platform for intracellular interfacing to neuronal circuits. *Nature Nanotechnology* **7**, 180–184 (2012).
- Xie, C., Lin, Z., Hanson, L., Cui, Y. & Cui, B. Intracellular recording of action potentials by nanopillar electroporation. *Nature Nanotechnology* **7**, 185–190 (2004).
- Maze, J. R. *et al.* Nanoscale magnetic sensing with an individual electronic spin in diamond. *Nature* **455**, 644–U41 (2008).
- Balasubramanian, G. *et al.* Nanoscale imaging magnetometry with diamond spins under ambient conditions. *Nature* **455**, 648–U46 (2008).
- Steinert, S. *et al.* High sensitivity magnetic imaging using an array of spins in diamond. *Rev. Sci. Instrum.* **81** (2010).
- McGuinness, L. P. *et al.* Quantum measurement and orientation tracking of fluorescent nanodiamonds inside living cells. *Nat. Nanotech.* **6**, 358363 (2011).
- Specht, C. G., Williams, O. A., Jackman, R. B. & Schoepfer, R. Ordered growth of neurons on diamond. *Biomaterials* **25**, 4073–4078 (2004).
- Yu, S. J., Kang, M. W., Chang, H. C., Chen, K. M. & Yu, Y. C. Bright fluorescent nanodiamonds: No photobleaching and low cytotoxicity. *J. Am. Chem. Soc.* **127**, 17604–17605 (2005).
- Royeck, M. *et al.* Role of axonal Na^+ 1.6 sodium channels in action potential initiation of Ca^{2+} pyramidal neurons. *J. Neurophys.* **100**, 2361–2380 (2008).
- Wimmer, V. C., Reid, C. A., So, E. Y. W., Berkovic, S. F. & Petrou, S. Axon initial segment dysfunction in epilepsy. *J. Phys. Lon.* **588**, 1829–1840 (2010).
- Wimmer, V. C. *et al.* Axon initial segment dysfunction in a mouse model of genetic epilepsy with febrile seizures plus. *J. Clin. Invest.* **120**, 2661–2671 (2010).
- Sabharwal, Y. Digital camera technology for scientific bio-imaging. *Micr. Anal.* **84** (2011).
- Watanabe, A. & Grundfest, H. Impulse propagation at the septal and commissural junctions of crayfish lateral axons. *J. Gen. Physiol.* **45**, 267–308 (1961).
- Degen, C. L. Scanning magnetic field microscope with a diamond single-spin sensor. *Appl. Phys. Lett.* **92**, 3 (2008).
- Taylor, J. M. *et al.* High-sensitivity diamond magnetometer with nanoscale resolution. *Nat. Phys.* **4**, 810–816 (2008).

- Schoenfeld, R. S. & Harneit, W. Real time magnetic field sensing and imaging using a single spin in diamond. *Phys. Rev. Lett.* **106** (2011).
- Cole, J. H. & Hollenberg, L. C. L. Scanning quantum decoherence microscopy. *Nanotechnology* **20**, 10 (2009).
- Hall, L. T., Cole, J. H., Hill, C. D. & Hollenberg, L. C. L. Sensing of fluctuating nanoscale magnetic fields using nitrogen-vacancy centers in diamond. *Phys. Rev. Lett.* **103** (2009).
- Laraoui, A., Hodges, J. S. & Meriles, C. A. Magnetometry of random ac magnetic fields using a single nitrogen-vacancy center. *Appl. Phys. Lett.* **97** (2010).
- Neugart, F. *et al.* Dynamics of diamond nanoparticles in solution and cells. *Nano Lett.* **7**, 3588–3591 (2007).
- Fu, C. C. *et al.* Characterization and application of single fluorescent nanodiamonds as cellular biomarkers. *Proc. Natl. Acad. Sci. USA* **104**, 727–732 (2007).
- Chao, J. I. *et al.* Nanometer-sized diamond particle as a probe for biolabeling. *Biophys. J.* **93**, 2199–2208 (2007).
- Faklaris, O. *et al.* Detection of single photoluminescent diamond nanoparticles in cells and study of the internalization pathway. *Small* **4**, 2236–2239 (2008).
- Hall, L. T. *et al.* Monitoring ion-channel function in real time through quantum decoherence. *Proc. Natl. Acad. Sci. USA* **107**, 18777–18782 (2010).
- Stanwix, P. L. *et al.* Coherence of nitrogen-vacancy electronic spin ensembles in diamond. *Phys. Rev. B* **82** (2010).
- Naydenov, B. *et al.* Enhanced generation of single optically active spins in diamond by ion implantation. *Appl. Phys. Lett.* **96** (2010).
- Pezzagna, S., Naydenov, B., Jelezko, F., Wrachtrup, J. & Meijer, J. Creation efficiency of nitrogen-vacancy centres in diamond. *New J. Phys.* **12** (2010).
- Naydenov, B. *et al.* Dynamical decoupling of a single-electron spin at room temperature. *Phys. Rev. B* **83**(8), 081201(R) (2011).
- Uhrig, G. S. *Phys. Rev. Lett.* **98**, 100504 (2007).
- Hall, L. T., Hill, C. D., Cole, J. H. & Hollenberg, L. C. L. Ultrasensitive diamond magnetometry using optimal dynamic decoupling. *Phys. Rev. B* **82**, 045208 (2010).
- Acosta, V. *et al.* Diamonds with a high density of nitrogen-vacancy centers for magnetometry applications. *Phys. Rev. B* **80**, 115202 (2009).
- Balasubramanian, G. *et al.* Ultralong spin coherence time in isotopically engineered diamond. *Nature Mater.* **8**, 383–387 (2009).
- Devoret, M. H. & Schoelkopf, R. J. Amplifying quantum signals with the single-electron transistor. *Nature* **406**(6799), 1039–1046 (2000).
- Dolde, F. *et al.* Electric-field sensing using single diamond spins. *Nat. Phys.* **7**, 459463 (2011).
- Childress, L. *et al.* Coherent dynamics of coupled electron and nuclear spin qubits in diamond. *Science* **314**, 281–285 (2006).

Acknowledgments

LCLH was supported by the Australian research Council through a Professorial Fellowship (DP0770715) and SP was funded by a NMHRC Fellowship (1005050) and Program Grant (628952). This work was also supported by the University of Melbourne through the Centre for Neural Engineering and the Centre for Neuroscience, and by the Victorian Government through the Operational Infrastructure Scheme. The authors would like to acknowledge K. Ganesan for assistance preparing the microwave striplines and A. Stacey for helpful discussions.

Author contributions

LTH, LCLH and JC developed the NV detection protocol and neuron signal analysis; GB, LTH, ET, SP performed the neuron simulations; DS, LMcG, RS, FJ, JW and LCLH were responsible for the measurements; all authors contributed to writing the paper. The project was conceived and directed by LCLH.

Additional information

Competing financial interests: The authors declare no competing financial interests.

License: This work is licensed under a Creative Commons Attribution-NonCommercial-ShareAlike 3.0 Unported License. To view a copy of this license, visit <http://creativecommons.org/licenses/by-nc-sa/3.0/>

How to cite this article: Hall, L. T. *et al.* High spatial and temporal resolution wide-field imaging of neuron activity using quantum NV-diamond. *Sci. Rep.* **2**, 401; DOI:10.1038/srep00401 (2012).